RSC Advances

PAPER

View Article Online
View Journal | View Issue

Cite this: *RSC Adv.*, 2023, **13**, 24077

Fabrication and properties of Sn(IV) porphyrin-linked porous organic polymer for environmental applications†

Chang-Ju Lee, Nirmal Kumar Shee and Hee-Joon Kim *

Received 19th June 2023
Accepted 7th August 2023

DOI: 10.1039/d3ra04117d

rsc.li/rsc-advances

A robust porous organic polymer cross-linked by Sn(IV) porphyrin (**SnPOP**) was fabricated by reacting *trans*-dihydroxo-[5,15,10,20-tetrakis(phenyl)porphyrinato]tin(IV) (SnP) with fluorinated polyimide (FPI) *via* sol–gel formation, followed by supercritical CO_2 drying. The structural and porous properties of SnPOP were characterized using FT-IR, UV-vis, and fluorescence spectroscopies, along with field-emission scanning electron microscopy and gas sorption experiments. The reaction between the SnP's oxophilic Sn(IV) center and FPI's carboxylic acid moiety resulted in a controllable cross-linked porous texture. This material features the desirable physical properties of porphyrin and exhibits mesoporous structures with a relatively high surface area. **SnPOP** is thermally stable at temperatures up to 600 °C and highly resistant to boiling water, strong acids, and bases, owing to its assembly *via* formation of covalent bonds instead of typically weaker hydrogen bonds. The modified chemical and morphological structures of **SnPOP** showed an impressive CO_2 uptake capacity of 58.48 mg g^{-1} at 273 K, with a preference for CO_2 over N_2. **SnPOP** showed significant efficiency in removing pollutant dyes, such as methylene blue and methyl orange, from dye-contaminated water. Additionally, **SnPOP** was a photocatalyst for fabricating silver nanoparticles of regular shape and size. All these properties make **SnPOP** a potential candidate for environmental applications like pollutant removal, gas storage, and separation.

Introduction

Soft microporous materials, such as metal–organic frameworks (MOFs),[1] porous coordination polymers (PCPs),[2] covalent organic frameworks (COFs),[3] and porous organic polymers (POPs),[4] have attracted significant attention owing to their valuable features. These features include superior thermal and chemical stabilities, large accessible surface areas, insoluble backbones, tunable porosities, and various functionalities. The multidimensional properties of these materials make them good alternatives to classical porous materials, such as zeolites,[5] metal oxides,[6] ceramics,[7] mesoporous silica,[8] and activated charcoal.[9] These materials have been extensively studied and utilized in various fields including heterogeneous catalysis,[10] gas storage,[11] biomedicine,[12] gas separation,[13] water purification,[14] electrochemistry,[15] and sensing.[16] POPs, which are highly cross-linked amorphous porous materials, are typically characterized by ample molecular-scale porosity (pore diameters ranging from a few nanometers to micrometers). The porosity of these materials not only increases the catalytic activity by increasing the number of reactant-accessible catalyst sites but also adsorbs reactant molecules, thereby boosting catalytic reaction rates. Unlike MOFs, POPs are purely organic and are usually constructed using complementary pairs of rigid organic building blocks *via* strong covalent bonds.[17–20] Among the various building blocks used in the fabrication of porous materials, porphyrin compounds are increasingly adopted because of their ability to translate building blocks into well-defined structures with regular pores. Porphyrins show excellent optical absorption properties in the visible region because of the presence of conjugated π electrons. Furthermore, they exhibit excellent absorption and electron transfer properties and are widely used in photocatalysis.[21–23] Monomeric porphyrinic compounds are self-assembled into nano and micro-architectures *via* supramolecular noncovalent interactions, such as hydrogen bonds, π–π stacking, and van der Waals interaction. Moreover, their intriguing structures and flexible cavities allow for easy control of the active sides, facilitating the understanding of structure–property relationships.[24–26] In this context, herein we report the synthesis and characterization of a porphyrin-based porous organic polymer (**SnPOP**) using metallated porphyrin as a cross-linker *via* a sol–gel route (Scheme 1).

Sn(IV) porphyrin (SnP) was selected as the source of porphyrin compounds because of its unique optical properties and octahedral geometries. Owing to the oxophilic nature of the

Department of Chemistry and Bioscience, Kumoh National Institute of Technology, Gumi 39177, Republic of Korea. E-mail: hjk@kumoh.ac.kr

† Electronic supplementary information (ESI) available: Additional characterization data and information. See DOI: https://doi.org/10.1039/d3ra04117d

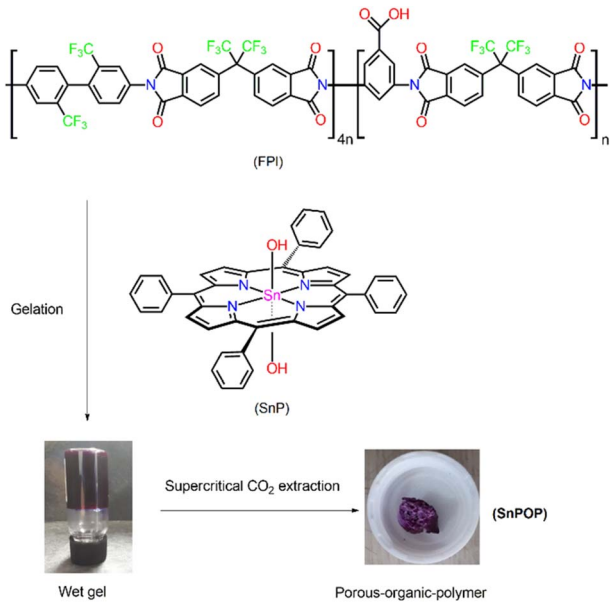

Scheme 1 Synthesis of Sn(IV) porphyrin-linked porous organic polymer (**SnPOP**).

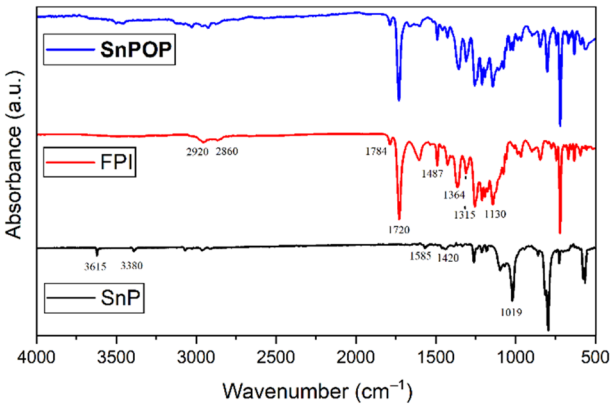

Fig. 1 FT-IR spectra of SnP, FPI, and **SnPOP**.

Sn(IV) center, Sn(IV) porphyrin can readily form stable six-coordinated complexes with two oxyanions (carboxylates or alkoxides) in the *trans* position. This advantageous tuning capability of SnPs makes them ideal scaffolds for constructing coordination complexes,[27–35] nanostructures,[36–44] and multi-porphyrin arrays,[45–47] which exhibit characteristic functions. Sn(IV)-porphyrin-based supramolecular nanostructures have been extensively studied as photocatalysts for wastewater remediation.[48,49] Fluorinated polyimide (FPI) was used as the source of the organic polymer skeleton because of its chemical and physical stability. Our designed porous organic polymer (**SnPOP**) material utilizes SnP gelators to fabricate porous materials using the supercritical carbon dioxide extraction method.[50–53] This is a promising method for fabricating porphyrin-based porous materials. Importantly, **SnPOP** is expected to retain the original properties of the SnPs and organic polymers to the maximum extent possible. The spectral features of **SnPOP** were successfully characterized, and its useful properties for environmental applications were studied. These properties include gas sorption capacities for N_2 and CO_2, dye removal abilities, and photocatalytic fabrication of metal nanoparticles.

Results and discussion

Syntheses and spectroscopic characterization

The design and the synthetic scheme of **SnPOP** are schematically illustrated in Scheme 1. Typically, a dichloromethane (DCM) solution of SnP was mixed with a dimethylformamide (DMF) solution of FPI, and the mixture was incubated in the dark to obtain a wet gel. Throughout the experiment, we made several interesting observations to optimize the reaction conditions in terms of solvent systems, reaction time, and concentration of the starting materials. Initially, solvent-dependent analysis revealed that the gel formation was successful in a DMF–DCM mixture (1 : 1), and partial gel formation occurred in DMF–THF (tetrahydrofuran). However, no gel was formed when only DMF was used. Additionally, we observed that low concentrations of starting materials ($\sim 10^{-4}$ to 10^{-5} M) are best for wet gel formation. Gel formation began after 24 h, and the optimal time for complete gel formation was fixed at 72 h. After 72 h, the wet gel was immersed in DCM several times to remove DMF and unreacted SnP. Subsequently, the wet gel was dried using supercritical CO_2 at high pressure and temperature to form porous **SnPOP**. The strong affinity of the axial hydroxyl ligand of SnP towards the carboxylic group of FPI led to the formation of a cross-linked polymer. FT-IR spectra of SnP, FPI, and **SnPOP** are shown in Fig. 1.

In the case of SnP, the absorption peaks at 1019 cm^{-1} corresponded to the bending vibrations of $C(sp^2)$–H in planar aromatic ring. On the other hand, out-of-plane bending vibrations of $C(sp^2)$–H of the aromatic rings appeared at 794 cm^{-1}. The peaks at 3380, 1585, and 1420 cm^{-1} were assigned to the stretching vibrations of C–H, C=C, and C–N, respectively, in the pyrrole ring. Furthermore, the peaks at 3615 cm^{-1} were attributed to the stretching vibrations of the O–H signal of the axial hydroxyl group in SnP. On the other hand, FPI exhibited two bands at 2920 and 2860 cm^{-1} belonging to the O–H stretching vibration of the carboxylic acid group. Additionally, the two bands at 1784 and 1720 cm^{-1} were attributed to the symmetric and asymmetric stretching vibrations of the carbonyl group of the imide ring. Furthermore, the bands at 1487 and 1364 cm^{-1} corresponded to the C–N stretching vibration and the aromatic ring, respectively. The characteristic bands of the CF_3 group in FPI were observed in the region of 1315–1130 cm^{-1}. The FT-IR spectrum of **SnPOP** clearly showed that the peak corresponding to O–H stretching at $\sim$3615 cm^{-1} completely vanished, confirming the complete reaction of the axial hydroxyl group of SnP with the carboxylic group of FPI. All other peaks remained unchanged or changed slightly compared with those of the starting components. These observations indicated the strong attachment of SnP to FPI to form **SnPOP**.

The solid-state UV-vis spectroscopy in Nujol was used to characterize the light absorption properties of SnP, FPI, and

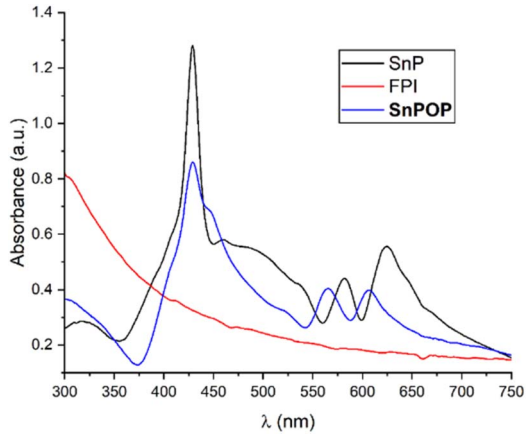

Fig. 2 Solid state UV-vis absorption spectra of SnP, FPI, and **SnPOP** in Nujol.

SnPOP (Fig. 2). SnP shows a strong light absorption peak at 428 nm corresponding to the Soret band, along with two weaker absorption peaks at 582 and 624 nm corresponding to the Q bands. On the other hand, FPI did not show any strong absorbance bands in the visible region. In comparison to SnP, **SnPOP** displayed a strong light absorption peak at 428 nm for the Soret band, as well as two weaker peaks at 565 and 605 nm for the Q bands. This result implied that the Q bands in SnP experienced a blue-shift, thereby confirming the strong attachment of SnP to **SnPOP**.

The solid-state fluorescence spectra of SnP, FPI, and **SnPOP** were recorded (Fig. 3). SnP displays broad emission peaks at 602 and 650 nm at an excitation wavelength of 550 nm. FPI, however, did not show any fluorescence signal. In contrast, **SnPOP** exhibited emission peaks at 615 and 653 nm. The emission peak-to-peak ratio of SnP changed to that of **SnPOP**, suggesting a strong attachment.

The morphological characteristics of **SnPOP** were evaluated by field-emission scanning electron microscopy (FE-SEM). The

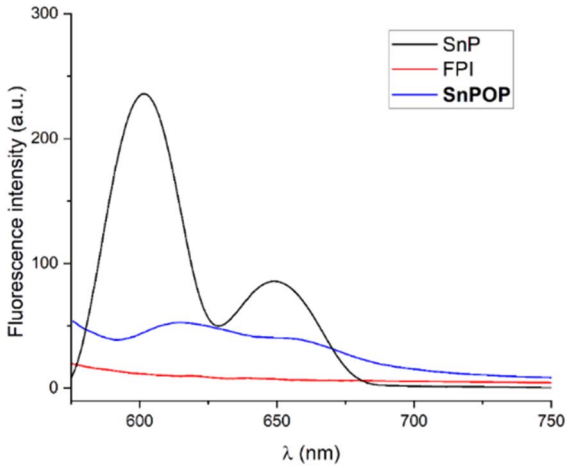

Fig. 3 Solid state fluorescence (λ_{ex} = 550 nm) spectra of SnP, FPI, and **SnPOP** in Nujol.

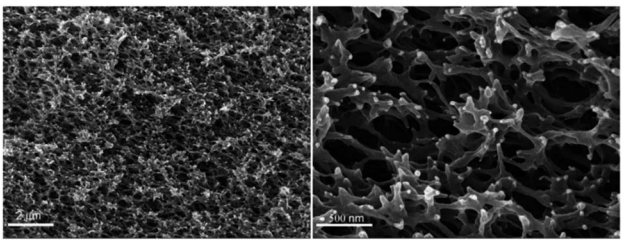

Fig. 4 Low- and high-resolution FE-SEM images for **SnPOP**.

FE-SEM images clearly showed a two-dimensional fibrous sponge-like structure with interconnected bonds (Fig. 4).

The sponges were smooth and flat, with an average length and width of approximately 400 and 50 nm, respectively. Irregularly arranged strips resembling those observed throughout the foamy sponge skeleton consisted of a classic discontinuous network of interpenetrating open and porous channels. The pore sizes of the larger scaffolds were cross-linked with an average diameter ranging between 260 and 350 nm, whereas the smaller channels had an average diameter ranging between 70 and 160 nm.

Similar to crystalline polyarylether-based COFs,[54] amorphous **SnPOP** displays high thermal and chemical stabilities. The thermogravimetric analysis (TGA) curves of **SnPOP** are shown in Fig. S1.† The first change in the curve (between 100 and 200 °C) corresponded to the removal of physically adsorbed water on the surface, accounting for ~3% of the total mass loss. Enormous weight losses (~43%) were observed at around 612 °C, which was attributed to the elimination of surface-bound organic groups in **SnPOP**. These observations indicated that **SnPOP** was thermally stable at temperatures up to ~600 °C. Interestingly, SnP underwent dramatic weight loss starting only at 350 °C.[55] To investigate the chemical stability of **SnPOP**, different chemical environments, including different aqueous and organic solvents, were used to expose the **SnPOP** samples for 24 h. It was observed that **SnPOP** swelled in THF, DCM, acetone, and ethyl acetate, while retaining its gel form (Fig. S2†). In contrast, **SnPOP** retained its original skeleton and porous networks even after treatment with NaOH (10 M), HCl (10 M), or boiling water, as demonstrated by the morphology of **SnPOP** (Fig. S3a–c†). However, when immersed in aprotic polar solvents, such as DMF and DMAc, **SnPOP** lost its original skeleton and porous framework (Fig. S3d†).

Gas sorption

To study the porous properties of **SnPOP**, N_2 adsorption and desorption analyses were performed at 77 K after degasification at 200 °C for 12 h to remove the adsorbed molecules. The adsorption and desorption isotherms of N_2 for **SnPOP** are shown in (Fig. 5).

The N_2 sorption isotherms of **SnPOP** exhibited a combination of type I and II isotherms, along with strong adsorption at low pressures (P/P_0 < 0.1), suggesting that mesopores and micropores coexist in the framework. The BET-specific surface area of **SnPOP** was calculated to be 227.2 $m^2\ g^{-1}$. To further

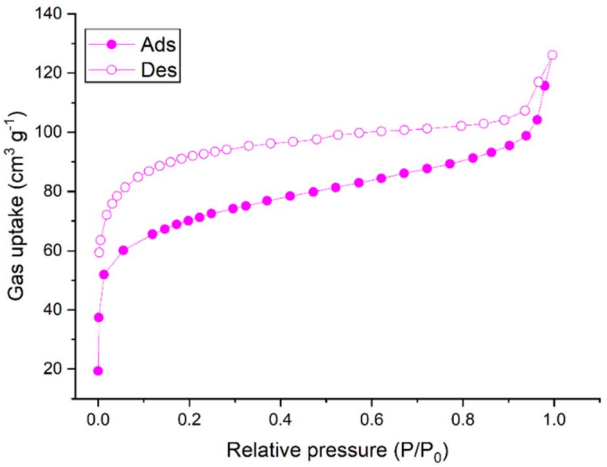

Fig. 5 Adsorption and desorption isotherms of N_2 for **SnPOP** at 77 K.

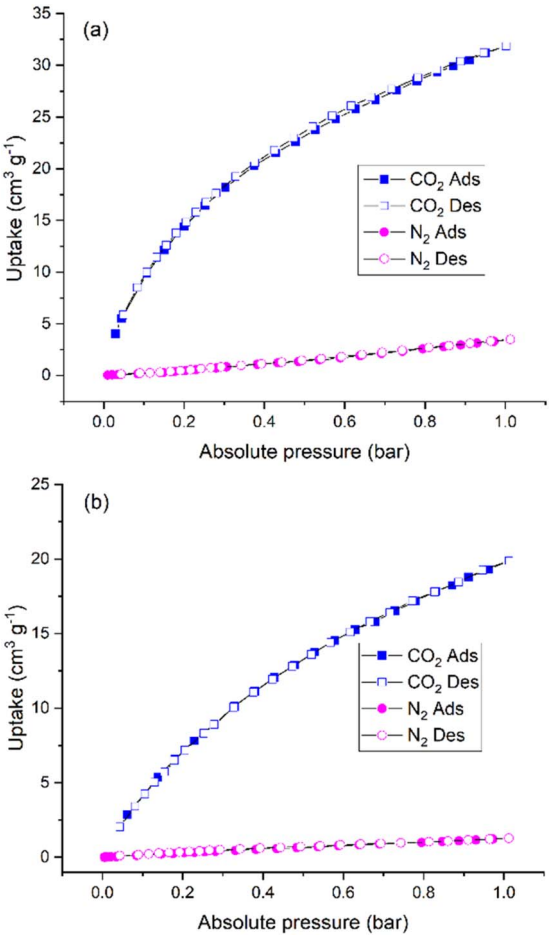

Fig. 6 CO_2 and N_2 sorption isotherms for **SnPOP** at 273 K (a) and 298 K (b).

confirm the pore size of **SnPOP**, the pore size distribution (PSD) plots calculated from the adsorption branch of the isotherms using the Non-local density functional theory (NLDFT) method are shown in Fig. S2.† The PSD of **SnPOP** was mostly centered at ~2.04 nm. The specific surface area value of **SnPOP** was determined using the relative pressure (P/P_0) range of 0.01–0.10.

Considering the high porosity, we studied the potential applications of **SnPOP** for CO_2 adsorption and separation. The adsorption isotherms of CO_2, and N_2 were measured at 273 and 298 K, respectively. As shown in Fig. 6, the sorption amounts of CO_2 are as high as 31.85 cm^3 g^{-1} (58.48 mg g^{-1}) at 273 K and 19.89 cm^3 g^{-1} (36.52 mg g^{-1}) at 298 K.

All sorption isotherms revealed moderate CO_2 adsorption, comparable to those reported for porphyrin-based porous materials (Table S1†). Meanwhile, the CO_2 uptake is much higher than N_2 uptake (3.48 cm^3 g^{-1} or 4.35 mg g^{-1} at 273 K, and 1.27 cm^3 g^{-1} or 1.59 mg g^{-1} at 298 K). The isotherms for both gases at 273 and 298 K demonstrated no uptake in the low-concentration region, but gradually increased adsorption at higher concentrations. We further calculated the CO_2/N_2 selectivity based on the experimental conditions. The ideal adsorption selectivity of SnPOP was calculated using the following equation:[56]

$$\alpha_{12}^{\mathrm{abs}} = (N_1^{\mathrm{ads}}/N_2^{\mathrm{ads}})(y_2/y_1)$$

where N is the absorbed amount, y is the mole fraction, α is the ideal adsorption selectivity coefficient, and subscripts 1 and 2 indicate stronger (CO_2) and weaker absorbent (N_2), respectively.

For example, the ideal adsorption selectivity of **SnPOP** was found to be as high as 21.2 for CO_2/N_2 at 273 K and 23.1 for CO_2/N_2 at 298 K. The selectivity of **SnPOP** at similar temperatures was comparable to or higher than that of recently reported porphyrin-based porous materials. The absorption isotherms clearly showed that **SnPOP** selectively absorbed CO_2 over N_2,[13,57,58] which can be attributed to the dipole–quadrupole interaction between the organic functional groups present in **SnPOP** and the guest CO_2 molecules. The dispersion force within CO_2 molecules was significantly affected by their quadrupole moment or polarizability.

Dye adsorption

To assess the adsorption capacity of **SnPOP** for bulky molecule transportation, azo dyes were selected. Specifically, we selected the anionic dye methyl orange (MO) and cationic dye methylene blue (MB). Approximately 20 mg of **SnPOP** was mixed with 100 mL aqueous solution of dye (50 mg L^{-1}) and continuously stirred for 5 h at room temperature in the dark. Subsequently, the solid particles were separated from the solution through centrifugation. The residual concentrations of the dyes were determined by UV-vis spectroscopy after dilution, and calculated according to the standard curve. It can be seen in Fig. 7 and 8, **SnPOP** exhibited outstanding adsorption both for MB and MO with removal efficiencies of 75% and 70%, respectively. As shown in Fig. S3 and S4,† **SnPOP** showed a higher uptake capacity of cationic dye (187.5 mg g^{-1} for MB) compared to anionic dye (175 mg g^{-1} for MO). These results demonstrate that the porphyrin-linked porous **SnPOP** materials have a fairly high capability for dye adsorption and are comparable to reported porphyrin-based porous materials (Table S2†).

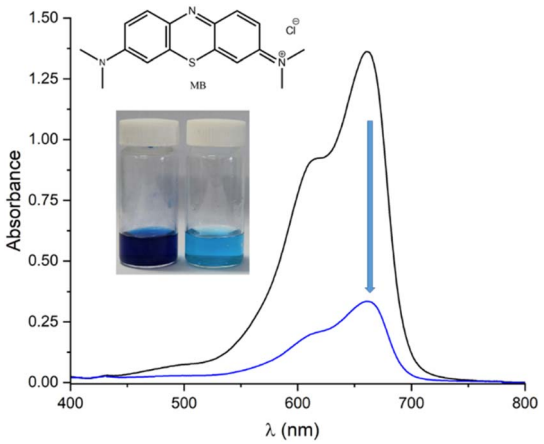

Fig. 7 UV-vis absorption spectral change of methylene blue (MB) in water upon **SnPOP** treatment.

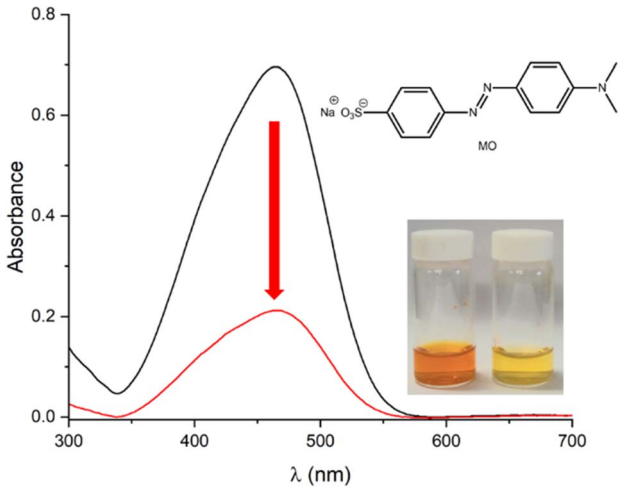

Fig. 8 UV-vis absorption spectral change of methyl orange (MO) in water upon **SnPOP** treatment.

Photocatalytic fabrication of Ag nanoparticles

Currently, silver nanostructures have received considerable attention because of their reduced density, increased surface area, and unique electronic and optical properties, which have led to a wide range of important applications in biosensing,[59] catalysis,[60] photochemistry,[61] and photodynamic therapy.[62] Among others, the photochemical method is the most suitable process for controlling the morphology of metal nanostructures and their tunable properties for enhanced applications. In this method, researchers use the direct chemical reduction of a metal precursor to fabricate metal nanostructures.[63] Occasionally, photosensitizers are used as intermediate species.[64] Shelnutt *et al.* observed that SnP can reduce Pt(II) ion species to Pt nanoparticles (NPs) with well-defined shapes and uniform sizes under visible light irradiation.[65] Additionally, Pereira *et al.* reported a facile photoredox process for fabricating Au and Ag NPs from a water-soluble Sn(IV) porphyrin complex.[66] Inspired by previous observations, we used **SnPOP** as a photoredox catalyst to fabricate Ag NPs under visible light irradiation.

The photocatalytic method described in Scheme 2 was used to synthesize Ag NPs. The photocatalyst used in this study was the Sn(IV) porphyrin-linked porous polymer, **SnPOP**. Photocatalytic reduction of silver salts occurred in the presence of visible light and the electron donor triethylamine (TEA). The absorption of visible light by **SnPOP** yields a long-lived excited triplet π–π* state, **SnPOP***, which is rapidly reduced by an ED such as TEA. The resulting product is a long-lived radical ion, $\mathbf{SnPOP}^{-\bullet}$, which is a strong reductant capable of effectively reducing Ag^{+} to Ag^{0}. The reduction of the metal regenerates neutral **SnPOP**, which can then absorb light and initiate a successive photochemical cycle. The photocatalytic cycle is reductive because the initial electron transfer event involves the reduction of the porphyrin anion by TEA. It is important to note that we did not use any capping agent like poly(*N*-vinyl pyrrolidone) (PVP) or any surfactants.[53,55] The use of surfactants such as sodium dodecyl sulphate (SDS) makes it difficult to separate Ag NPs from the reaction mixture. We examined the optical and surface properties of the as-prepared Ag NPs using UV-vis spectrophotometry, FE-SEM/EDS, and TEM.

The surface morphology and size of the synthesized Ag NPs on SnPOP were observed by FE-SEM and the images are shown in Fig. S4.† The Ag NPs exhibited regular and homogeneous structures, with almost spherical shapes and diameters of 15–60 nm (Fig. S5†). Additionally, agglomerated growth of Ag NPs was observed, with an estimated particle size ranging from 150 to 400 nm and clear boundaries. To confirm the formation of the synthesized Ag NPs energy-dispersive X-ray spectroscopy (EDX) was performed. The EDX analysis was performed to examine the elemental composition, homogeneity, and distribution of the as-prepared Ag NPs. As shown in Fig. S6,† the EDX spectrum confirms the presence of Ag NPs on **SnPOP.** A strong signal in the Ag region is evident, indicating the formation or creation of Ag NPs at approximately 3.1 keV. Furthermore, the

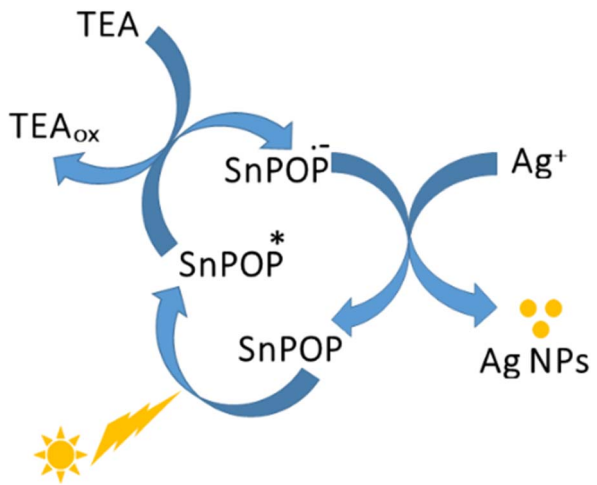

Scheme 2 Photocatalytic reaction cycle for the synthesis of silver nanoparticles (Ag NPs) from the silver cations in the presence of **SnPOP** at room temperature.

presence of weak absorption signals for carbon and oxygen were observed at approximately 0.24 and 0.49 keV, respectively.

Experimental

Materials and methods

All commercial chemicals were used as received, unless otherwise specified. Toluene and pyrrole were distilled from the calcium hydride solution. The synthesis of *trans*-dihydroxo-[5,15,10,20-tetraphenylporphyrinato]tin(IV) (SnP) followed a previously reported procedure.[67] FPI was synthesized according to the reported procedure.[68] Elemental analysis was performed using a ThermoQuest EA 1110 analyzer. Steady-state UV-vis spectra were recorded using a Shimadzu UV-3600 spectrophotometer (Shimadzu, Tokyo, Japan). Fluorescence spectra were recorded using a Shimadzu RF-5301PC fluorescence spectrophotometer (Shimadzu, Tokyo, Japan). Fourier transform infrared (FT-IR) spectra (KBr) were obtained using a Shimadzu FTIR-8400S spectrophotometer (Shimadzu, Tokyo, Japan). Thermogravimetric analysis (TGA) was performed using an Auto-TGA Q500 instrument (TA Instruments, New Castle, DE, USA) under nitrogen. The Brunauer–Emmett–Teller (BET) surface area was determined with an analyzer (BELSORP-mini volumetric adsorption equipment) using N_2 adsorption isotherms at 77 K. Surface and pore size data were obtained using Autosorb-iQ and Quadrasorb SI. Field-emission scanning electron microscopy (FE-SEM) images were obtained using a MAIA III instrument (TESCAN, Brno, Czech Republic).

Synthesis of Sn(IV) porphyrin-linked porous organic polymer

A 5 mL dichloromethane (DCM) solution of SnP (6.5×10^{-5} M) was mixed with 5 mL of dimethylformamide (DMF) solution of FPI (1.3×10^{-4} M) in a sample vial. The solution was kept in a dark at room temperature (298 K) for gelation. After 3 days, a wet gel was formed. The wet gels were then subjected to solvent exchange for 24 h to remove DMF and unreacted SnP three times in succession by immersing in DCM. Subsequently, the wet gel was dried using supercritical CO_2 at 333 K and 100 bar for 6 h. After the autoclave was depressurized slowly at room temperature for about 6 h, a **SnPOP** was obtained.

Photocatalytic fabrication of Ag nanoparticles using Sn(IV) porphyrin-linked porous organic polymer

A 5 mL acetonitrile solution of silver nitrate (9 mM) and TEA was mixed in a 20 mL glass vial. To this solution, 50 mg **SnPOP** was added, and the reaction system was subjected to stirring at room temperature while being irradiated with a xenon bulb at a power of 50 W for 1 h. At the end of the reaction, the color of the **SnPOP** changed from purple to blue, suggesting the formation of Ag nanoparticles. The solution was decanted from the reaction mixture and the product was dried *in vacuo*.

Conclusions

We developed a robust **SnPOP** by reacting SnP with FPI. The fabrication process of **SnPOP** consists of two steps. First, a wet gel was formed by reacting SnP with FPI in DMF-DCM at room temperature. In the second step, the wet gel was transformed into **SnPOP** with high porosity through extraction with supercritical CO_2. The reaction between the oxophilic Sn(IV) center in SnP and the carboxylic acid functional group of FPI resulted in a controllable cross-linked porous texture. More importantly, the intrinsic properties of SnP and organic polymer were likely to be maximally retained in **SnPOP**. **SnPOP** is thermally stable up to 600 °C and extremely resistant to various chemical environments, including boiling water, strong acids, and bases. This is because of the covalent bond formation during the assembly of **SnPOP**, which is stronger than the typically weaker hydrogen bonds. Moreover, this material features the attractive properties of porphyrins and exhibits mesoporous structures with a relatively high surface area. The modified chemical and morphological structures in **SnPOP** showed an impressive CO_2 uptake capacity of 58.48 mg g^{-1} at 273 K and enable preferential CO_2 uptake over N_2. **SnPOP** showed a significant ability to remove pollutant dyes, such as MB and MO, from dye-contaminated water. In addition, **SnPOP** has been used as a photocatalyst for the fabrication of Ag nanoparticles with regular shape and size. In conclusion, our report on Sn(IV) porphyrin-linked organic polymers provides valuable insights into the development of various stable functional materials with high porosity for environmental applications, such as pollutant removal, gas storage, and separation.

Author contributions

Data curation, investigation, methodology, C.-J. L.; formal analysis, software, validation, visualization, and writing, N. K. S.; conceptualization, funding acquisition, project administration, review, resources, supervision, validation, and editing, H.-J. K.

Conflicts of interest

There are no conflicts to be declared.

Acknowledgements

This study was supported by the National Research Foundation of Korea (NRF) (grant no. 2022R1F1A1074420) funded by the Korean government (MSIT).

References

1 H. Li, M. Eddaoudi, M. O'Keeffe and O. M. Yaghi, Design and synthesis of an exceptionally stable and highly porous metal–organic framework, *Nature*, 1999, **402**, 276–279.
2 S. Kitagawa, R. Kitaura and S. I. Noro, Functional porous coordination polymers, *Angew. Chem., Int. Ed.*, 2004, **43**, 2334–2375.
3 A. P. Côté, A. I. Benin, N. W. Ockwig, M. O'Keeffe, A. I. Matzger and O. M. Yaghi, Porous, Crystalline, Covalent Organic Frameworks, *Science*, 2005, **310**, 1166–1170.

4 P. Kaur, J. T. Hupp and S. T. Nguyen, Porous Organic Polymers in Catalysis: Opportunities and Challenges, *ACS Catal.*, 2011, **1**, 819–835.
5 Z. Cao, X. Cai, A. C. Feltrin, P. Feng, A. Kaiser and F. Akhtar, Calcium/strontium chloride impregnated zeolite A and X granules as optimized ammonia sorbents, *RSC Adv.*, 2022, **12**, 34910–34917.
6 L. Wang, C. Shi, L. Pan, X. Zhang and J.-J. Zou, Rational design, synthesis, adsorption principles and applications of metal oxide adsorbents: a review, *Nanoscale*, 2020, **12**, 4790–4815.
7 Z. Yang, H. Liang, L. Jin and D. Poelman, High-performance lead-free bulk ceramics for electrical energy storage applications: design strategies and challenges, *J. Mater. Chem. A*, 2021, **9**, 18026–18085.
8 M. Iranshahy, M. Y. Hanafi-Bojd, S. H. Aghili, M. Iranshahi, S. M. Nabavi, S. Saberi, R. Filosa, I. F. Nezhad and M. Hasanpour, Curcumin-loaded mesoporous silica nanoparticles for drug delivery: synthesis, biological assays and therapeutic potential – a review, *RSC Adv.*, 2023, **13**, 22250–22267.
9 L. Yang, W. Yungang, L. Tao, Z. Li, B. Yanyuan and X. Haoran, High-performance sorbents from ionic liquid activated walnut shell carbon: an investigation of adsorption and regeneration, *RSC Adv.*, 2023, **13**, 22744–22757.
10 C. Perego and R. Millinib, Porous Materials in Catalysis: Challenges for Mesoporous Materials, *Chem. Soc. Rev.*, 2013, **42**, 3956–3976.
11 H. Li, L. Li, R.-B. Lin, W. Zhou, Z. Zhang, S. Xiang and B. Chen, Porous Metal-Organic Frameworks for Gas Storage and Separation: Status and Challenges, *EnergyChem*, 2019, **1**, 100006.
12 S. K. Das, S. Mishra, K. D. Saha, D. Chandra, M. Hara, A. A. Mostafa and A. Bhaumik, N-Rich, Polyphenolic Porous Organic Polymer and Its *In Vitro* Anticancer Activity on Colorectal Cancer, *Molecules*, 2022, **27**, 7326.
13 N. K. Shee, C.-J. Lee and H.-J. Kim, Hexacoordinated Sn(IV) porphyrin-based square-grid frameworks exhibiting selective uptake of CO_2 over N_2, *Bull. Korean Chem. Soc.*, 2022, **43**, 103–109.
14 N. K. Shee, H. J. Jo and H.-J. Kim, Coordination framework materials fabricated by the self-assembly of Sn(IV) porphyrins with Ag(I) ions for the photocatalytic degradation of organic dyes in wastewater, *Inorg. Chem. Front.*, 2022, **9**, 1270–1280.
15 D. H. Yang, Y. Tao, X. Ding and B. H. Han, Porous Organic Polymers for Electrocatalysis, *Chem. Soc. Rev.*, 2022, **51**, 761–791.
16 Z.-W. Li, B. Tan, Z.-F. Wu and X.-Y. Huang, A Robust Strontium Coordination Polymer with Selective and Sensitive Fluorescence Sensing Ability for Fe^{3+} Ions, *Materials*, 2023, **16**, 577.
17 Y. Zhang and S. N. Riduan, Functional porous organic polymers for heterogeneous catalysis, *Chem. Soc. Rev.*, 2012, **41**, 2083–2094.
18 M. Inukai, M. Tamura, S. Horike, M. Higuchi, S. Kitagawa and K. Nakamura, Storage of CO_2 into Porous Coordination Polymer Controlled by Molecular Rotor Dynamics, *Angew. Chem., Int. Ed.*, 2018, **57**, 8687–8690.
19 T. Zhang, G. Xing, W. Chen and L. Chen, Porous organic polymers: a promising platform for efficient photocatalysis, *Mater. Chem. Front.*, 2020, **4**, 332–353.
20 Z. Xu, L. Hu, J. Ming, X. Cui, M. Zhang, J. Dou, W. Zhang and B. Zhou, Self-Gated Porous Organic Polymer as Drug Delivery System for PH Stimuli-Responsive Controlled Quercetin Release, *Microporous Mesoporous Mater.*, 2020, **303**, 110259.
21 X. W. Jiang, Y. F. Liu, J. Liu, Y. L. Luo and Y. Lyu, Facile synthesis of porous organic polymers bifunctionalized with azo and porphyrin groups, *RSC Adv.*, 2015, **5**, 98508–98513.
22 T. Hasobe, Supramolecular nanoarchitectures for light energy conversion, *Phys. Chem. Chem. Phys.*, 2010, **12**, 44–57.
23 A. M. Kobaisy, M. F. Elkady, A. A. Abdel-Moneim and M. E. El-Khouly, Surface-decorated porphyrinic zirconium-based metal–organic frameworks (MOFs) using post-synthetic self-assembly for photodegradation of methyl orange dye, *RSC Adv.*, 2023, **13**, 23050–23060.
24 I. Beletskaya, V. S. Tyurin, A. Y. Tsivadze, R. Guilard and C. Stern, Supramolecular chemistry of metalloporphyrins, *Chem. Rev.*, 2009, **109**, 1659–1713.
25 S. Durot, J. Taesch and V. Heitz, Multiporphyrinic Cages: Architectures and Functions, *Chem. Rev.*, 2014, **114**, 8542–8578.
26 N. K. Shee, J.-W. Seo and H.-J. Kim, Spectrophotometric Study of Bridging N-Donor Ligand-Induced Supramolecular Assembly of Conjugated Zn-Trisporphyrin with a Triphenylamine Core, *Molecules*, 2021, **26**, 4771.
27 H. J. Kim, K.-M. Park, T. K. Ahn, S. K. Kim, K. S. Kim, D. Kim and H.-J. Kim, Novel fullerene–porphyrin–fullerene triad linked by metal axial coordination: Synthesis, X-ray crystal structure, and spectroscopic characterizations of trans-bis([60]fullerenoacetato)tin(iv) porphyrin, *Chem. Commun.*, 2004, 2594–2595.
28 H.-J. Kim, H. J. Jo, J. Kim, S.-Y. Kim, D. Kim and K. Kim, Supramolecular self-assembly of tin(IV) porphyrin channels stabilizing single-file chains of water molecules, *CrystEngComm*, 2005, **7**, 417–420.
29 H. J. Kim, W. S. Jeon, J. H. Lim, C. S. Hong and H.-J. Kim, Synthesis, X-ray crystal structure, and electrochemistry of *trans*-bis(ferrocenecarboxylato)(tetraphenylporphyrinato) tin(IV), *Polyhedron*, 2007, **26**, 2517–2522.
30 H. J. Kim, J. H. Jang, H. Choi, T. Lee, J. Ko, M. Yoon and H.-J. Kim, Photoregulated Fluorescence Switching in Axially-Coordinated Tin(IV) Porphyrinic Dithienylethene, *Inorg. Chem.*, 2008, **47**, 2411–2415.
31 W. Kim, T. Tachikawa, T. Majima, C. Li, H.-J. Kim and W. Choi, Tin-porphyrin sensitized TiO_2 for the production of H_2 under visible light, *Energy Environ. Sci.*, 2010, **3**, 1789–1795.
32 H. J. Jo, S. H. Kim and H.-J. Kim, Supramolecular Assembly of Tin(IV) Porphyrin Cations Stabilized by Ionic Hydrogen-Bonding Interactions, *Bull. Korean Chem. Soc.*, 2015, **36**, 2348–2351.

33 N. K. Shee, M. K. Kim and H.-J. Kim, Fluorescent chemosensing for aromatic compounds by supramolecular complex composed of tin(IV) porphyrin, viologen, and cucurbit[8]uril, *Chem. Commun.*, 2019, **55**, 10575–10578.

34 M. K. Kim, N. K. Shee, J. Lee, M. Yoon and H.-J. Kim, Photoinduced Electron Transfer upon Supramolecular Complexation of (Porphyrinato) Sn-Viologen with Cucurbit [7] uril, *Photochem. Photobiol. Sci.*, 2019, **18**, 1996–2002.

35 N. K. Shee, C.-J. Lee and H.-J. Kim, Crystal structure of bis (benzoato-κO)[5,15-di-phenyl-10,20-bis(pyridin-4-yl) porphyrinato-κ^4N,N′,N″,N‴]tin(IV), *IUCrData*, 2019, **4**, x190787.

36 S. J. Lee, R. A. Jensen, C. D. Malliakas, M. G. Kanatzidis, J. T. Hupp and S. T. Nguyen, Effect of secondary substituent on the physical properties, crystal structures, and nanoparticle morphologies of (porphyrin)$Sn(OH)_2$: diversity enabled *via* synthetic manipulations, *J. Mater. Chem.*, 2008, **18**, 3640–3642.

37 C. J. Medforth, Z. Wang, K. E. Martin, Y. Song, J. L. Jacobsen and J. A. Shelnutt, Self-assembled porphyrin nanostructures, *Chem. Commun.*, 2009, 7261–7277.

38 C. Li, K.-M. Park and H.-J. Kim, Ionic assembled hybrid nanoparticle consisting of tin(IV) porphyrin cations and polyoxomolybdate anions, and photocatalytic hydrogen production by its visible light sensitization, *Inorg. Chem. Commun.*, 2015, **60**, 8–11.

39 N. K. Shee, M. K. Kim and H.-J. Kim, Supramolecular Porphyrin Nanostructures Based on Coordination-Driven Self-Assembly and Their Visible Light Catalytic Degradation of Methylene Blue Dye, *Nanomaterials*, 2020, **10**, 2314.

40 N. K. Shee and H.-J. Kim, Self-Assembled Nanomaterials Based on Complementary Sn(IV) and Zn(II)-Porphyrins, and Their Photocatalytic Degradation for Rhodamine B Dye, *Molecules*, 2021, **26**, 3598.

41 N. K. Shee and H.-J. Kim, Morphology-controlled self-assembled nanostructures of complementary metalloporphyrin triads through intermolecular coordination tuning and their photocatalytic degradation for Orange II, *Inorg. Chem. Front.*, 2022, **9**, 5538–5548.

42 N. K. Shee and H.-J. Kim, Sn(IV)-Porphyrin-Based Nanostructures Featuring Pd(II)-Mediated Supramolecular Arrays and Their Photocatalytic Degradation of Acid Orange 7 Dye, *Int. J. Mol. Sci.*, 2022, **23**, 13702.

43 S. H. Kim and H.-J. Kim, Photocatalytic Hydrogen Production by the Sensitization of Sn(IV)-Porphyrin Embedded in a Nafion Matrix Coated on TiO_2, *Molecules*, 2022, **27**, 3770.

44 N. K. Shee and H.-J. Kim, Supramolecular squares of Sn(iv) porphyrins with Re(i)-corners for the fabrication of self-assembled nanostructures performing photocatalytic degradation of Eriochrome Black T dye, *Inorg. Chem. Front.*, 2023, **10**, 174–183.

45 H.-J. Kim, N. Bampos and J. K. M. Sanders, Assembly of Dynamic Heterometallic Oligoporphyrins Using Cooperative Zinc-Nitrogen, Ru-Nitrogen and Tin-Oxygen Coordination, *J. Am. Chem. Soc.*, 1999, **121**, 8120–8121.

46 M. T. Indelli, C. Chiorboli, M. Ghirotti, M. Orlandi, F. Scandola, H. J. Kim and H.-J. Kim, Photoinduced Electron Transfer in Ruthenium(II)/Tin(IV) Multiporphyrin Arrays, *J. Phys. Chem. B*, 2010, **114**, 14273–14282.

47 H. J. Kim, N. K. Shee, K. M. Park and H.-J. Kim, Assembly and X-ray crystal structures of heterometallic multiporphyrins with complementary coordination between ruthenium(II) and tin(IV) porphyrins, *Inorg. Chim. Acta*, 2019, **488**, 1–7.

48 N. K. Shee and H.-J. Kim, Three Isomeric Zn(II)-Sn(IV)-Zn(II) Porphyrin-Triad-Based Supramolecular Nanoarchitectures for the Morphology-Dependent Photocatalytic Degradation of Methyl Orange, *ACS Omega*, 2022, **7**, 9775–9784.

49 N. K. Shee and H.-J. Kim, Sn(IV) Porphyrin-Based Ionic Self-Assembled Nanostructures and Their Application in Visible Light Photo-Degradation of Malachite Green, *Catalysts*, 2022, **12**, 799.

50 X. Zhao, L. Yuan, Z.-Q. Zhang, Y.-S. Wang, Q. Yu and J. Li, Synthetic Methodology for the Fabrication of Porous Porphyrin Materials with Metal–Organic–Polymer Aerogels, *Inorg. Chem.*, 2016, **55**, 5287–5296.

51 X. Xu, Q. Yu, D. Zhao, W. Zhang, N. Wang and J. Li, Synthesis and characterization of porphyrin-based porous coordination polymers obtained by supercritical CO_2 extraction, *J. Mater. Sci.*, 2018, **53**, 10534–11054.

52 W. Zhang, J. J. Dynes, Y. Hu, P. Jiang and S. Ma, Porous metal-metalloporphyrin gel as catalytic binding pocket for highly efficient synergistic catalysis, *Nat. Commun.*, 2019, **10**, 1913.

53 Y. Keum, B. Kim, A. Byun and J. Park, Synthesis and Photocatalytic Properties of Titanium-Porphyrinic Aerogels, *Angew. Chem., Int. Ed.*, 2020, **59**, 21591–21596.

54 X. Guan, H. Li, Y. Ma, M. Xue, Q. Fang, Y. Yan, V. Valtchev and S. Qiu, Chemically stable polyarylether-based covalent organic frameworks, *Nat. Chem.*, 2019, **11**, 587–594.

55 N. K. Shee, B.-H. Park and H.-J. Kim, Hybrid Composite of Sn(IV)-Porphyrin and Mesoporous Structure for Enhanced Visible Light Photocatalytic Degradation of Organic Dyes, *Molecules*, 2023, **28**, 1886.

56 Y. S. Bae and R. Q. Snurr, Development and evaluation of porous materials for carbon dioxide separation and capture, *Angew. Chem., Int. Ed.*, 2011, **50**, 11586–11596.

57 Z. Wang, S. Yuan, A. Mason, B. Reprogle, D. J. Liu and L. Yu, Nanoporous porphyrin polymers for gas storage and separation, *Macromolecules*, 2012, **45**, 7413–7419.

58 N. Huang, R. Krishna and D. Jiang, Tailor-Made Pore Surface Engineering in Covalent Organic Frameworks: Systematic Functionalization for Performance Screening, *J. Am. Chem. Soc.*, 2015, **137**, 7079–7082.

59 W. S. T. Tun, S. Kulchat, C. Talodthaisong, S. Daduang, J. Daduang, K. Rongchai and R. Patramanon, A machine learning colorimetric biosensor based on acetylcholinesterase and silver nanoparticles for the detection of dichlorvos pesticides, *Mater. Chem. Front.*, 2022, **6**, 1487–1498.

60 A. Shen, R. Luo, X. Liao, C. He and Y. Li, Highly dispersed silver nanoparticles confined in a nitrogen-containing

covalent organic framework for 4-nitrophenol reduction, *Mater. Chem. Front.*, 2021, **5**, 6923–6930.

61 D. Gola, A. Kriti, N. Bhatt, M. Bajpai, A. Singh, A. Arya, N. Chauhan, S. K. Srivastava, P. K. Tyagi and Y. Agrawal, Silver nanoparticles for enhanced dye degradation, *Curr. Res. Green Sustainable Chem.*, 2021, **4**, 100132.

62 M. T. Yaraki, Y. Pan, F. Hu, Y. Yu, B. Liu and Y. N. Tan, Nanosilver-enhanced AIE photosensitizer for simultaneous bioimaging and photodynamic therapy, *Mater. Chem. Front.*, 2020, **4**, 3074–3085.

63 H. Wang, X. Qiao, J. Chen and S. Ding, Preparation of silver nanoparticles by chemical reduction method, *Colloids Surf., A*, 2005, **256**, 111–115.

64 F. Bai, Z. Sun, H. Wu, R. E. Haddad, X. Xiao and H. Fan, Templated Photocatalytic Synthesis of Well-Defined Platinum Hollow Nanostructures with Enhanced Catalytic Performance for Methanol Oxidation, *Nano Lett.*, 2011, **11**, 3759–3762.

65 Y. Song, Y. Yang, C. J. Medforth, E. Pereira, A. K. Singh, H. Xu, Y. Jiang, C. J. Brinker, F. van Swol and J. A. Shelnutt, Controlled synthesis of 2-D and 3-D dendritic platinum nanostructures, *J. Am. Chem. Soc.*, 2004, **126**, 635–645.

66 P. Quaresma, L. Soares, L. Contar, A. Miranda, I. Osorio, P. A. Carvalho, R. Franco and E. Pereira, Green photocatalytic synthesis of stable Au and Ag nanoparticles, *Green Chem.*, 2009, **11**, 1889–1893.

67 H. J. Jo, S. H. Jung and H.-J. Kim, Synthesis and Hydrogen-Bonded Supramolecular Assembly of *trans*-Dihydroxotin(IV) Tetrapyridylporphyrin Complexes, *Bull. Korean Chem. Soc.*, 2004, **25**, 1869–1873.

68 H. Q. Pham, G. Kim, H. M. Jung and S.-W. Song, Fluorinated Polyimide as a Novel High-Voltage Binder for High-Capacity Cathode of Lithium-Ion Batteries, *Adv. Funct. Mater.*, 2018, **28**, 1704690.